Journal of Natural Remedies
DOI: 10.18311/jnr/2026/55802

INFORMATICS JOURNALS
Research Article
eISSN: 2320-3358 | Vol 26(7), 2026 | pp. 1905-1922

In Silico Evaluation of *Dichrostachys cinerea* Phytochemicals Against Alzheimer's Disease: Network Pharmacology and Molecular Dynamics Insights

Prabhakar Vengadasamy and A. Vijayalakshmi*

Department of Pharmacognosy, School of Pharmaceutical Sciences, Vels Institute of Science Technology and Advanced Studies (VISTAS), Pallavaram, Chennai - 600117, Tamil Nadu, India; avijibaskaran@gmail.com

Abstract

Background: Alzheimer's disease (AD) affects over 55 million individuals worldwide, and current therapies offer only symptomatic relief without modifying disease progression. The complex, multi-factorial pathology of AD — involving neuroinflammation, oxidative stress, tau hyperphosphorylation, and amyloid-β accumulation — demands a multi-target therapeutic strategy. *Dichrostachys cinerea*, a plant with well-documented ethnomedicinal use, presents unexplored neuroprotective potential. **Aim:** To investigate the multi-target anti-Alzheimer's potential of phytochemicals derived from *D. cinerea* using an integrated computational approach combining GC-MS profiling, network pharmacology, molecular docking, and molecular dynamics simulation. **Methods:** GC-MS analysis of the hydroethanolic extract identified 134 metabolites, which were subjected to drug-likeness and ADMET screening. Network pharmacology was performed using SwissTargetPrediction and GeneCards to identify 249 common AD-related targets. PPI network analysis via STRING and CytoHubba identified hub genes. Molecular docking was carried out using AutoDock Vina against IL6 (PDB: 1ALU), GSK3β (PDB: 1Q5K), and PPARG (PDB: 6MS7). Molecular dynamics (MD) simulations were performed for 100 ns using GROMACS. **Results:** Among 134 identified metabolites, 92.5% exhibited favourable drug-like properties. Network analysis revealed IL6, PPARG, and GSK3β as key hub targets among 249 overlapping AD-related genes. Andrographolide demonstrated the highest binding affinities across all three targets (IL6: −8.4 kcal/mol; GSK3β: −8.8 kcal/mol; PPARG: −8.4 kcal/mol). MD simulations confirmed superior stability of the andrographolide–GSK3β complex with consistent RMSD convergence and persistent hydrogen bonding throughout 100 ns. **Conclusion:** This study provides the first systems-level computational evidence for *D. cinerea's* multi-target therapeutic potential in AD, establishing a molecular foundation for future experimental validation.

Major Findings: Andrographolide from *D. cinerea* showed strong, stable binding to IL6, GSK3β, and PPARG—key AD hub targets. The andrographolide–GSK3β complex had the best docking score (−8.8 kcal/mol) and greatest MD stability over 100 ns.

Keywords: Alzheimer's Disease, Andrographolide, *Dichrostachys cinerea*, Molecular Dynamics, Network Pharmacology, Neuroinflammation

(Article Chronicle: Article Received on: 12.04.2026; Revised on: 04.06.2026; Accepted on: 06.07.2026)

1. Introduction

Alzheimer's disease (AD) is one of the most pressing health crises today, affecting over 55 million people worldwide and posing substantial challenges for families, healthcare institutions, and society as a whole[1,2]. An AD patient suffers from a heartbreaking progression of the disease: loss of memory, cognitive

*Author for correspondence

function and independence. On a cellular level, the disease is a consequence of the hyperphosphorylated tau and amyloid-β plaques, which are toxic, and chronic inflammation of the brain tissue[3,4].

After decades of research and the expenditure of billions of dollars, progress has been made, although it has been very modest, as current therapies are very ineffective, simply providing coverage of symptoms on a temporary basis, and absolutely no treatment is available that interrupts progress or reverses the disease[5]. The problem is that AD is extremely complex; it has no one singular cause; virtually all of the systems involved function imperfectly, including chronic inflammation, oxidative stress, energy deficits in neurons, loss of synaptic connections, and protein misfolding[6,7]. Traditional drug development, which targets a single molecule, has time and time again proven ineffective, identifying an increasingly critical need for the development of more rational approaches that can address multiple systems of disease simultaneously[8,9].

In contrast to traditional approaches, network pharmacology accounts for the intricacies of ailments such as AD by determining drug interactions across multiple targets within the frameworks of various biological networks, corresponding to how diseases function *in vivo*[10-12]. *Dichrostachys cinerea* has been employed in traditional African medicine for several years as a medicinal plant for various ailments. Even though this plant has been used for a long time, from the point of view of science, it has been assumed to be of little or no importance in the understanding of how it might protect the brain from degenerative diseases[13,14].

The use of modern computational science has transformed the way in which we design drugs since it allows the systematic prediction and analysis of molecular interactions at a level that was previously unattainable. Network pharmacology integrates the diverse fields of chemistry, systems biology and network theory to answer the question of how natural products function holistically. This technique is especially useful because the majority of plant medicines function through multiple components[15–17].

The current work undertaken was to determine whether the phytochemicals obtained from the plant, *D. cinerea*, possess any therapeutic activity in the management of AD through the use of integrated network pharmacology methods. The use of GC-MS chemical profiling, in conjunction with computational target prediction, molecular docking and molecular dynamics, and network and functional enrichment analyses, sought to construct a multi-target systems-level understanding of how *D. cinerea* compounds may affect the counterment of AD. These results provide a molecular basis for new lab work and may assist in the formulation of new multi-targeted therapies for this devastating disease.

2. Materials and Methods

2.1 Collection and Extraction

The leaves of *D. cinerea* were collected during the month of October 2025 and authenticated by the Siddha Medicinal Plants Garden, Mettur (sample code D260625044C). Extraction was performed by maceration using a hydroethanolic solvent system (ethanol: water, 70:30 v/v). The resulting extract was concentrated under reduced pressure using a rotary evaporator to obtain the final hydroethanolic extract[18-20].

2.2 Phytochemical Profiling via GC-MS

Chemical characterisation of the extract employed GC-MS analysis on an Agilent 7890A system coupled with a 5975C mass detector, utilising an HP-5MS fused silica column (30 m × 0.25 mm i.d., 0.25 µm film). Operating parameters: initial temperature 60°C (2 min), ramped at 10°C/min to 280°C (5 min hold), helium carrier gas (1.2 mL/min), EI mode (70 eV), scan range m/z 50-550. Metabolite identification involved spectral matching against NIST 17 and Wiley libraries with ≥85% similarity threshold[21-25].

2.3 Drug-likeness Assessment

Pharmacokinetic properties were computationally evaluated using SwissADME. Parameters assessed included Lipinski descriptors, TPSA, rotatable bonds, and oral bioavailability. Synthetic feasibility was determined through SAScore calculations (1-10 scale), where lower values indicate easier synthesis routes[26-31].

2.4 Network Pharmacology

The screening of potential target genes for the phytochemicals of *D. cinerea* against AD was performed through a systematic network pharmacology workflow.

Initially, the SwissTarget Prediction platform was employed to predict putative targets of the phytochemicals, restricted to *Homo sapiens*, using their SMILES notation as input. To identify disease-associated genes, the GeneCards database was queried for AD–related targets. The predicted phytochemical targets were subsequently intersected with the AD gene set, generating a pool of common targets, which were further refined and analysed using the InteractiVenn web server. We used the DAVID bioinformatics tool (Database for Annotation, Visualisation, and Integrated Discovery) for Gene Ontology (GO) and KEGG pathway enrichment analyses as part of our study of how well our systems work. We looked at Biological Processes (BP), Molecular Functions (MF), and Cellular Components (CC). A modified p-value of ≤ 0.05 was utilised, concentrating on the top 10 of each GO term and KEGG pathway. Using Cytoscape v.3.10.0, we visualised the bioactive compounds and their target genes as nodes and their relationships as edges, representing the bipartite network of the phytochemicals and their targets in the pathway. Important nodes were selected based on the degree of their structural centrality and connectivity. A protein-protein interaction (PPI) network was derived from STRING to analyse the interconnectivity of the target proteins. This network was further analysed through Cytoscape with the help of the CytoHubba plugin to determine the primary regulatory nodes and hub genes, which in turn were used to identify the most significant targets hypothesised to confer the neuroprotective effects of *D. cinerea*[32-40].

2.5 Molecular Docking Study

The chosen ligands were docked against the target proteins IL6, GSK3β, and PPARG. The crystal structures of IL6 (PDB ID: 1ALU; resolution: 1.90 Å), GSK3β (PDB ID: 1Q5K; resolution: 2.40 Å), and PPARG (PDB ID: 6MS7; resolution: 1.43 Å) were obtained from the RCSB Protein Data Bank (https://www.rcsb.org/). This database offers a comprehensive collection of curated, high-resolution 3D structures of proteins, nucleic acids, and macromolecular assemblies, facilitating structural visualisation and analysis. Before performing docking studies, all heteroatoms, water molecules, and additional chains were eliminated from the crystal structures using Molegro Molecular Viewer to ensure proper preparation of the target proteins. The active site of each protein was analysed using SCFBIO, IIT-Delhi. Molecular docking was carried out using AutoDock Vina to evaluate the optimal binding orientations of the ligands with their respective target proteins, aiming to identify conformations with the highest binding affinity. Non-bonded interactions, including hydrogen bonds, pi-alkyl, and pi-sigma interactions, were analysed for the generated protein–ligand complexes using Discovery Studio Visualizer to identify and select the complexes exhibiting the most favourable binding affinities[41-45].

2.6 Molecular Dynamics Simulation

Molecular dynamics (MD) simulations were carried out using GROMACS version 2022.2. The ligand–protein complex structures were built and saved in PDB format with the aid of PyMOL. For system preparation, protein topology files were created through the pdb2gmx module employing the CHARMM27 force field, while ligand topology parameters were generated using the SwissParam server. After topology generation, each complex was placed in a cubic simulation box filled with TIP3P water molecules, maintaining at least a 1 nm buffer around the protein surface, and periodic boundary conditions were imposed. The addition of Na^+ counterions produced charge neutrality. Before equilibration, the system was subjected to energy minimisation (50,000 steps, steepest descent method). A 100 ps NVT run at 300 K and a 100 ps NPT run were required for equilibration. The protein, ligand, water, and ions were coupled independently using the leapfrog algorithm. The Berendsen thermostat (τ = 0.1 ps) and barostat (τ = 2 ps) were used to regulate the temperature and pressure, respectively. Under NPT conditions, production MD was performed for 100 ns at 300 K and 1 bar with a pressure coupling applied at a time constant of 1 ps. The LINCS algorithm was used to constrain all bond lengths. Trajectory visualisation was performed using VMD 1.9.2, and post-simulation analyses were conducted with HeroMDAnalysis and Xmgrace 5.1.25[46-48].

3. Results and Discussion

3.1 Phytochemical Identification via GC-MS Analysis

GC-MS profiling of the hydroethanolic extract of *D. cinerea* identified 134 distinct metabolites (Figure 1

and Table 1). The predominance of phytoconstituents reflects the complex secondary metabolite profile commonly observed in *Fabaceae* plants.

3.2 Drug-likeness Assessment and ADMET Profiling

ADMET evaluation revealed favourable pharmacokinetic properties across the identified compounds. The majority (92.5%, n=124) exhibited zero Lipinski violations with molecular weights ranging from 72.15-382.65 g/mol. Most compounds demonstrated acceptable lipophilicity (90.3% with LogP ≤4.15), suitable TPSA values (88.1% ≤140 Å²), and high predicted gastrointestinal absorption (89.6%). Blood-brain barrier permeation was predicted for 58.2% of compounds, indicating potential CNS activity relevant to Alzheimer's treatment. Only 5.2% were predicted as P-glycoprotein substrates, minimising efflux resistance concerns. Synthetic accessibility scores ranged from 1.0 to 5.56, with andrographolide showing the highest complexity (5.06) due to its multiple chiral centres. The overall favourable ADMET profile suggests these phytochemicals possess suitable pharmacokinetic characteristics for multi-target therapeutic development against neurodegenerative diseases.

3.3 Screening of the Compounds

The screened phytocompounds were assigned a synthetic accessibility (SA) score to evaluate their potential for chemical synthesis. The SA score ranges from 1 (easy to synthesise) to 10 (hard to synthesise). From Table 2, all the selected compounds had SA scores that fall between 4.35 and 5.06, which indicates that they are moderate in ease of synthesis. Among the phytocompounds, Andrographolide (A2) had the

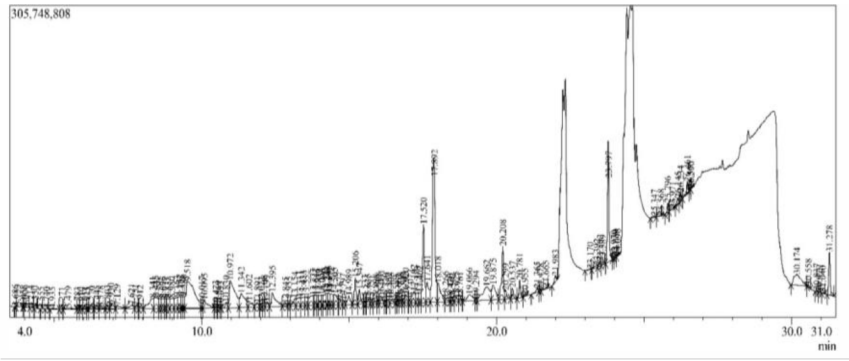


Figure 1. GC-MS chromatogram showing the metabolite profile of *Dichrostachys cinerea*.

Table 1. GC–MS identified phytocompounds

Peak	R. Time	Area	Height	Compound Name
1	3.686	189965	94049	Butane, 2-Methyl-
2	3.753	3651176	496584	Methyl 2-Oxopropanoate
3	3.958	23115	20597	1-(Bicyclo[2.2.1]hept-2-yl)ethanamine
4	4.006	797651	166191	3-(1-Methylethoxy)propanenitrile
5	4.214	791269	191571	2-Hydroxy-2-methyl-4-pentanone (Diacetone alcohol)
6	4.350	399602	109166	1,2-Dimethylbenzene
7	4.555	147943	57902	5-Amino-1-methyl-1H-imidazole-4-carboxylic acid
8	4.740	233854	94762	4-Methyl-1,2,5-oxadiazole-3-carboxylic acid
9	4.935	4215574	324418	1-(4-Hydroxy-5-Hydroxymethyl-Tetrahydro-Furan-2-Yl)-2
10	5.271	1066875	230423	3-Hydroxy-8-methyl-8-azabicyclo[3.2.1]octane-2-carboxylic acid (exo,exo)
11	5.479	21687018	1242845	2(3H)-Furanone, Dihydro-
12	5.783	1642307	368232	2-Carbamyl-9-[.Beta.-D-Ribofuranosyl] Hypoxanthine

Table 1. Continued...

Peak	R. Time	Area	Height	Compound Name
13	5.910	1429336	276036	5-Chloropentanoic Acid, 4-Methylpentyl Ester
14	6.051	4610320	670698	2(3H)-Furanone, 5-Methyl-
15	6.115	2283175	615870	N-Isopentyl-N-Nitroso-Pentylamine
16	6.270	9932812	1079686	Naphthalene-4a,8a-Dicarboxylic Acid, 1,4,4a,5,8,8a-Hexahydro-, Dimethyl Ester
17	6.445	16941183	1784690	2,4-Dihydroxy-2,5-Dimethyl-3(2H)-Furan-3-One
18	6.578	16158358	1665735	Butanoic Acid, 2-Methyl-5-Oxo-1-Cyclopenten-1-Yl Ester
19	6.803	13321048	2144094	Benzene, 1-Methyl-3-(1-Methylethyl)-
20	6.930	35618004	3982103	2-Oxabicyclo[2.2.2]Octane, 1,3,3-Trimethyl-
21	7.129	34954645	2734243	Oxabicyclo[2.2.2]Octane, 1,3,3-Trimethyl-
22	7.621	41183576	3299386	Threitol, 2-O-Octyl-
23	7.751	17166029	2534987	1-Butanol, 3-Methyl-
24	7.912	12534334	1621142	4-Aminobutyraldehyde Diethyl Acetal
25	8.341	116605632	9904419	Furaneol
26	8.445	112199382	10949906	Phenol, 4-Methoxy-
27	8.585	49679186	9911755	Bicyclo[2.2.1]Heptan-2-Ol, 1,3,3-Trimethyl-, (1R-Endo)-
28	8.676	54798487	9758076	Hexanal
29	8.777	43358081	9714583	N-(N-Propyl)-1,3-Propanediamine
30	8.835	62880985	9710313	2-Hexenal, (E)-
31	8.980	83532799	9804310	Phenylethyl Alcohol
32	9.163	74892267	10991575	Cyclohexaneethanol, Acetate
33	9.267	78673252	11601333	Z-8-Octadecen-1-Ol Acetate
34	9.326	41533333	11592836	Propanal, 2,3-Dihydroxy-
35	9.388	44901210	11561460	Alpha.-D4-Hexamethylene Oxide
36	9.518	546851607	26453279	4H-Pyran-4-One, 2,3-Dihydro-3,5-Dihydroxy-6-Methyl-
37	10.017	19618410	5375115	Megastigma-3,7(E),9-Triene
38	10.095	76681451	7868580	7-Decen-2-One
39	10.473	4500571	923083	Megastigma-7(E),9,13-Triene
40	10.569	1929395	551035	1-Cyclohexene-1-Carboxaldehyde, 2,6,6-Trimethyl-
41	10.633	299466	165582	Acetic Acid, 2-(2-Methoxyethyl) Hexyl Ester
42	10.830	35353504	5512853	1,2,2-D3-Cyclopentane-1,3-Trans-Diol
43	10.972	353882701	26805143	2,3-Dihydro-Benzofuran
44	11.342	167134292	13702161	Guanosine
45	11.602	51003176	6007879	Vitispirane
46	11.891	33387815	3889528	Phenol, 2-Methyl-5-(1-Methylethyl)-
47	12.022	16889768	3528543	Ascaridole Epoxide
48	12.108	22454160	4663679	3-Buten-2-Ol, 4-(2,6,6-Trimethyl-1-Cyclohexen-1-Yl)-
49	12.199	34316909	4801439	5-Isopropyl-2-Methylphenol
50	12.395	150168684	13778898	2-Methoxy-4-Vinylphenol
51	12.845	22743050	2657895	Pentanoic Acid, Octyl Ester
52	12.955	13262242	2676270	(E)-1-(2,3,6-Trimethylphenyl) Buta-1,3-Diene (Tpb,1)
53	13.154	46644517	7312069	Phenol, 2,6-Dimethoxy-

Table 1. Continued...

Peak	R. Time	Area	Height	Compound Name
54	13.311	74833123	8224673	Nonane, 1,1-Diethoxy-
55	13.433	72686277	8406260	Hexanenitrile
56	13.552	50565148	8475680	Hexadecane
57	13.777	101421357	9725975	9-[2-Deoxy-.Beta.-D-Ribohexopyranosyl] Purin-6(1H)-One
58	13.847	59663379	10264966	Bicyclo[8.1.0]Undeca-2,6-Diene,3,7,11,11-Tetramethyl-,(1r*,
59	13.916	28984623	9687319	Nipecotic Acid, 1-Methyl-, Methyl Ester
60	14.034	67354923	9916659	Acetic Acid, 3-Hydroxy-5,5-Dimethoxy-3-Methyl-Pentyl Ester
61	14.096	26513958	9837769	1-Bromo-2,2,3,3-Tetramethyl-1-(1-Propynyl) Cyclopropane
62	14.221	79564968	11553105	Ethanone, 1-(2,3-Dihydro-1,1-Dimethyl-1H-Inden-4-Yl)-
63	14.249	24151778	11530808	2,6-Dimethyl-6-Nitro-2-Hepten-4-One
64	14.306	58881777	12117181	Bicyclo[3,3,1]Non-2-Ene, 7-Oxa-2,8,9-Trimethyl-5-Acetoxymethyl-
65	14.372	68653480	10861556	3-(2-Isopropenyl-1-Cyclopropen-1-Yl)-3-Methyl-1-(2-Oxopro
66	14.505	84337023	10300542	Methyl 1,1-Dimethyl-2,3-Dihydro-1H-Inden-4-Yl Ketone
67	14.677	39429183	5717251	1,4-Benzenediol, 2-Methoxy-
68	14.797	23791960	4289947	Phenol, 2-Methoxy-4-(1-Propenyl)-
69	14.989	57451528	8283119	4a,8-Dimethyl-2-(Prop-1-En-2-Yl)-1,2,3,4,4a,5,6,7-Octahydronaphthalene
70	15.206	115920441	25951891	Naphthalene, Decahydro-4a-Methyl-1-Methylene-7-(1-Methyl
71	15.347	65107137	14327763	.Alpha.-Selinene
72	15.533	8759244	2249023	Cyclopropane, 1,1,2-Trimethyl-3-(2-Methyl-1-Propenyl)-
73	15.635	20978185	3393838	1-Ethyl-1,3,3-Trimethyl Indane
74	15.751	7621881	2004748	Tricyclo[4.1.0.0(3,5)]Heptane, 2-Isobutenyl-4,4,7,7-Tetramet
75	15.898	15442450	2609067	4a-Methyl Octahydro-1,5-Naphthalenedione
76	15.988	17785283	4112943	4aR,8aS)-4a-Methyl-1-Methylene-7-(Propan-2-Ylidene) Decahydronaphthalene
77	16.091	40971215	6823334	2(4H)-Benzofuranone, 5,6,7,7a-Tetrahydro-4,4,7a-Trimethyl
78	16.220	14988402	3538944	4-({[2-(2,2-Dimethyl-4-Phenyltetrahydro-2H-Pyran-4-Yl)-3-H
79	16.332	28720196	4182817	Mome Inositol
80	16.408	25040160	3904882	2-Ethyl-Norbornan-2-Ol
81	16.589	2859017	966458	Ethyl 4-(Acetylamino)-1,2,5-Oxadiazole-3-Carboxylate
82	16.662	9862853	2923141	1,2,4-Cyclopentanetrione, 3-(2-Pentenyl)-
83	16.738	15533084	3880972	Spiro[Androst-5-Ene-17,1'-Cyclobutan]-2'-One, 3-Hydroxy-, (3.Beta.,17.Beta.)-
84	16.844	18951463	4667572	9-Octadecenoic Acid (Z)-
85	16.920	51005970	8039447	1,2-Benzenedicarboxylic Acid, Diethyl Ester
86	17.072	32597306	6377058	Oleic Acid, Propyl Ester
87	17.192	77094323	10938779	5-Isopropenyl-2-Methylcyclopent-1-Ene Carboxaldehyde
88	17.310	56084551	9424133	Andrographolide
89	17.402	38996204	9690781	1,6-Octadiene, 3-Ethoxy-3,7-Dimethyl-
90	17.520	368469044	76338902	Naphthalenemethanol, 1,2,3,4,4a,5,6,7-Octahydro-.Alpha.,.Alpha.,4a,8-Tetramethyl
91	17.641	135571922	19758997	Agarospirol
92	17.892	921690883	119246298	2-Naphthalenemethanol, 1,2,3,4,4a,5,6,7-Octahydro-.Alpha.,.Alpha.,4a,8-Tetramethyl
93	18.018	146782086	18389891	Tetraneurin-A Diol

Table 1. Continued...

Peak	R. Time	Area	Height	Compound Name
94	18.266	20769755	3500001	1H-3a,7-Methanoazulen-6-Ol, Octahydro-3,6,8,8-Tetramethyl
95	18.430	3288385	1106303	4-(4-Hydroxy-2,2,6-Trimethyl-7-Oxa-Bicyclo[4.1.0]Hept-1-Yl)
96	18.502	6015151	1776624	.Gamma.-Eudesmol Acetate
97	18.625	17447258	3355733	Bicyclo[2.2.1]Heptane-2,3-Diol, 1,7,7-Trimethyl-, (Exo, Exo)-
98	18.761	11254727	2373922	2-Cyclohexen-1-One, 4-(3-Hydroxybutyl)-3,5,5-Trimethyl-
99	19.066	83066095	5869762	Meso-Inositol
100	19.294	12813934	2925560	2-(4-Methoxyphenyl)-4,6-Dimethyl-1,3-Oxathiane
101	19.662	225721219	13069181	Tetradecanoic Acid
102	19.875	138952803	14449008	2(4H)-Benzofuranone, 5,6,7,7a-Tetrahydro-6-Hydroxy-4,4,7a
103	20.208	220958706	51950044	Neophytadiene
104	20.299	46451195	8675582	(2E)-3,7,11,15-Tetramethyl-2-Hexadecene
105	20.537	36089937	10807100	2-Hexadecen-1-Ol, 3,7,11,15-Tetramethyl-, [R-[R,R-(E)]]-
106	20.781	61342862	17361553	3,7,11,15-Tetramethyl-2-Hexadecen-1-Ol
107	20.955	4404461	1336559	Pentadecanoic Acid
108	21.365	19353872	3545561	Butyl Undecyl Phthalate
109	21.478	3755994	944984	7,9-Di-tert-Butyl-1-Oxaspiro(4,5)Deca-6,9-Diene-2,8-Dione
110	21.665	9321890	1454191	Isophytol
111	21.983	23054882	5725738	Phthalic Acid, Butyl Undecyl Ester
112	23.170	4954778	684535	2,2,6-Trimethyl-1-[2-(2-Methyl-1,3-Dioxolan-2-Yl) Ethenyl]-7
113	23.392	16541843	1665344	1-Tetradecanol
114	23.502	23257020	4425758	Cis-9-Octadecenoic Acid
115	23.589	13466267	3091284	7,10,13-Hexadecatrienoic Acid, Methyl Ester
116	23.797	438212870	79551870	Oxirane, Hexadecyl-
117	23.970	6260580	1484379	Dimethyl (Ethenyl) Propoxysilane
118	24.030	5144225	1261696	9,12-Octadecadienoic Acid, 18-(Trimethylsiloxy)-, Methyl
119	24.096	740213	191694	Myo-Inositol, 4-C-Methyl-
120	25.347	8379588	1005881	17-Octadecynoic Acid, Methyl Ester
121	25.568	1350414	322556	2-Deoxy-D-Glucose
122	25.796	25792279	8891761	3-Cyclopentylpropionic Acid, 2-Dimethylamino Ethyl Ester
123	25.971	4067497	427477	2D-Methylhexanoic Acid Methyl Ester
124	26.145	22483829	4852256	Cis-9-Hexadecenal
125	26.234	27695170	8033183	9-Octadecenal, (Z)-
126	26.461	36559361	11009398	Cyclohexane, Eicosyl-
127	26.555	6219002	1742066	Nonanoic Acid, 5-Hydroxy-, .Delta.-Lactone
128	26.590	618152	497094	2-Thiazolidinimine, 3-Methyl-
129	30.174	175874117	10352488	Cis, Cis, Cis-7,10,13-Hexadecatrienal
130	30.558	4353922	1387310	7-Heptadecene, 1-Chloro-
131	30.837	4007576	1361492	Octadecanoic Acid, Ethyl Ester
132	30.929	898175	360168	Cis-9,10-Epoxyoctadecanamide
133	31.040	1756561	577467	Kauran-18-Al, 17-(Acetyloxy)-, (4.Beta.)-
134	31.278	137946907	41899107	Squalenes

highest SA score (5.06); thus, it is the most difficult to be synthesised as it has a highly oxygenated diterpenoid structure, and to make matters worse, it has several chiral centres. On the other hand, 7,9-Di-tert-butyl-1,4-dioxaspiro[4.5]deca-6,8-diene-2,8-dione (A5) had the lowest SA score (4.35), indicating that it has a simple structure, and thus, it is more easily synthesised. Moderate ease of synthesis (i.e., 4.5 and 4.56) was also indicated by intermediate SA scores of Vitispirane (A1) and Acarosipol (A3), respectively. Surprisingly, 1h-3a,7-Methanoazulen-6-ol, octahydro-3,6,8,8-tetramethyl (A4), had a score of 4.39, which also indicated moderate ease of synthesis. The conclusion from the SA analysis is that the selected phytocompounds have no highly complex and/or intractable molecules for synthesis. So, it can be stated that the phytocompounds, in general, are reasonably easy to synthesise.

From the SwissTarget database, 278 possible target genes linked to the phytochemicals in *D. cinerea* were located. Simultaneously, 15,505 AD-related genes were collected from the GeneCards database. Venn diagrams were used to determine the intersection of these two datasets, and the results showed 249 coinciding genes (Figure 2). These genes were the focus of the analysis as they were considered important hub targets related to AD.

Network topology analysis showed that IL6, PPARG, EGFR, HIF1A, ESR1, JUN, PTGS2, GSK3β, MMP9, and PARP1 (Figure 3) were the top ten hub genes that are probably involved in the therapeutic mechanisms of *D. cinerea* to AD. IL6, as a pro-inflammatory cytokine and a major driver of Alzheimer's neuroinflammation, has the highest degree (108) and betweenness centrality makes it a crucial central player in this disease. Metabolic control, neuroprotection, and cell survival are also important pathways related to PPARG and EGFR, as they were highly ranked as the most connected nodes. It is also possible that HIF1A

Table 2. Compound codes, phytochemical names, and synthetic accessibility of screened phytocompounds

Compound Code	PhytochemicalName	SMILE	Synthetic Accessibility
A1	Vitispirane	CC1CCC2(O1)C(=C)C=CCC2(C)C	4.5
A2	Andrographolide	C[C@@]12CC[C@H]([C@@]([C@H]1CCC(=C)[C@H]2C/C=C/3\[C@@H](COC3=O)O)(C)CO)O	5.06
A3	Agarospirol	C[C@@H]1CCC=C([C@@]12CC[C@H](C2)C(C)(C)O)C	4.56
A4	1h-3a,7-Methanoazulen-6-Ol, Octahydro-3,6,8,8-Tetramethyl	CC1CCC2C13CCC(C(C3)C2(C)C)(C)O	4.39
A5	7,9-Di-tert-butyl-1-oxaspiro(4,5)deca-6,9-diene-2,8-dione	CC(C)(C)C1=CC2(CCC(=O)O2)C=C(C1=O)C(C)(C)C	4.35

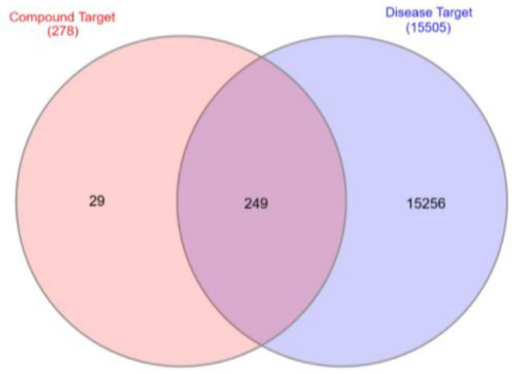


Figure 2. Disease and designed compound overlapping targets.

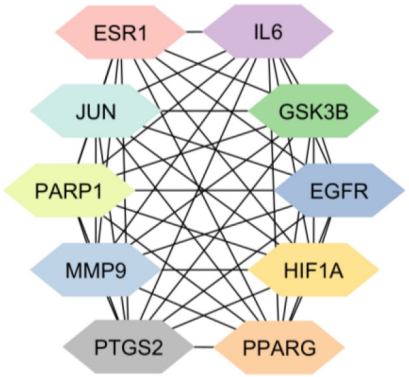


Figure 3. Visualisation of the top 10-ranked gene network.

and ESR1 are involved in both the hypoxia response and estrogen signalling, mechanisms that are known to relate to cognitive decline and the malfunction of neurons. It is also known that GSK3β, which is among the target genes, regulates tau phosphorylation. This aligns with the targets largely concerning AD.

MMP9 and PARP1 correspond with specific contributions of extracellular matrix remodelling and DNA repair/apoptosis, in contrast with JUN and PTGS2's focus on stress response and inflammatory cascades. Altogether, these hub genes exemplify inflammatory, metabolic, apoptotic, and neurodegenerative pathways, strengthening the multi-target, multi-pathway therapeutic value of *D. cinerea* in AD.

Network pharmacology analysis revealed a group of hub genes associated with Alzheimer's disease, from which the ten most influential targets were selected using centrality-based network parameters (Table 3). Among these, GSK3β stood out as the dominant hub, displaying the highest degree value (108) along with the greatest betweenness centrality (0.1277). This prominent network position reflects its involvement in major pathological events such as amyloid plaque formation, tau hyperphosphorylation, and extracellular matrix remodelling, reinforcing the contribution of inflammatory and neurodegenerative mechanisms to AD progression.

High network connectivity was also observed for IL6 (degree 86; betweenness centrality 0.0736) and EGFR (degree 84; betweenness centrality 0.0579). Their positioning within the network supports their established roles in neuroinflammatory signalling, oxidative stress regulation, and neuronal survival. In addition, HIF1A, ESR1, and JUN exhibited notable centrality values, suggesting that these genes contribute to maintaining network coherence and sustaining disease-associated signalling cascades.

By comparison, PTGS2 (COX-2) and MMP9 showed weaker interconnections within the network. PARP1, however, displayed a contrasting pattern, characterised by a low degree but a high clustering coefficient. This distribution implies participation in localised functional modules, potentially linked to DNA damage repair pathways and neuronal apoptosis. Taken together, these findings highlight EGFR, PPARG, and IL6 as key points of network integration in AD. The convergence of metabolic, neuroprotective, and inflammatory pathways emphasises the multifactorial nature of the disease and supports the rationale for a multi-target, phytochemical-based therapeutic strategy.

The compounds under investigation mainly targeted signalling networks associated with inflammation and cancer, as indicated by the KEGG pathway enrichment analysis(Figure 4). With the highest enrichment, the "Pathways in cancer" appear to be crucial in mediating the pharmacological effects. Furthermore, the signalling pathways for TNF and IL-17 were significantly enriched, suggesting their involvement in immune regulation and inflammation, two processes closely linked to the emergence of tumours and chronic diseases. Mechanistic evidence from pathways such as endocrine resistance and estrogen signalling supports the potential use of these substances in hormone-dependent cancers,

Table 3. Details of the top ten important target genes involved in Alzheimer's

Name	Betweenness Centrality	Closeness Centrality	Clustering Coefficient	Degree
GSK3β	0.127701244	0.633074935	0.181031499	108
IL6	0.073624634	0.586124402	0.206566347	86
PPARG	0.057885654	0.581947743	0.265347103	84
HIF1A	0.048627917	0.575117371	0.272314184	79
ESR1	0.071091387	0.584725537	0.262737263	78
JUN	0.03496755	0.565819861	0.306666667	76
PTGS2	0.056762132	0.568445476	0.235196687	70
EGFR	0.02880451	0.550561798	0.32568306	61
MMP9	0.019611451	0.534934498	0.324858757	60
PARP1	0.015905437	0.517970402	0.42743106	53

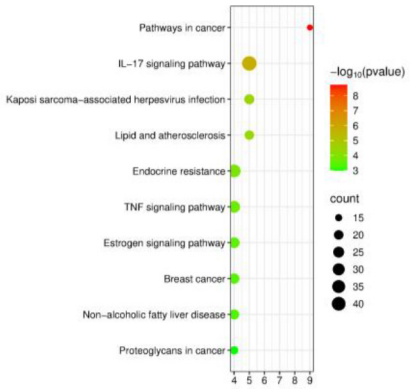


Figure 4. Results of KEGG enrichment analysis.

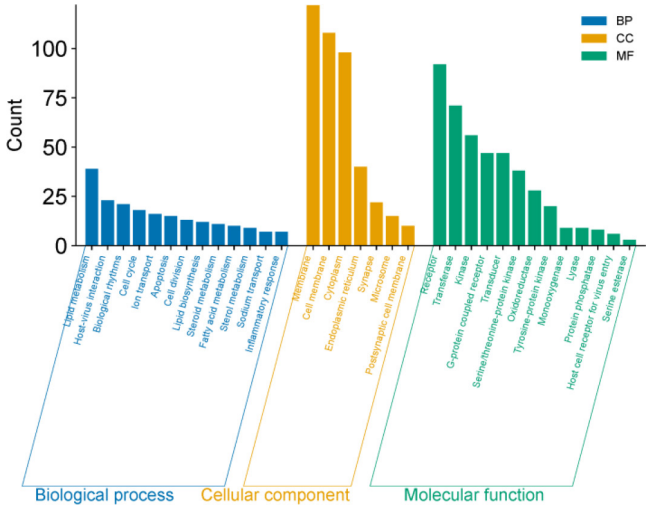


Figure 5. Results of GO enrichment analysis.

particularly breast cancer, which was also identified as an independent enriched pathway. Additionally, non-alcoholic fatty liver disease, Kaposi sarcoma-associated herpes virus infection, and the enrichment of lipid and atherosclerosis pathways suggest broader therapeutic potential that goes beyond oncology to viral and metabolic disorders. Overall, the results show that the compounds work through a multi-target, multi-pathway mechanism consistent with the systems-level approach of network pharmacology. By altering interrelated cancer, immune, and metabolic pathways, the compounds exhibit promise as multifunctional therapeutic agents with potential applications across a range of diseases.

The Gene Ontology (GO) enrichment analysis provided a detailed description of the biological processes, cellular components and molecular functions that were involved in the selected targets (Figure 5). These targets showed a considerable overrepresentation in lipid metabolism, host-virus interactions, circadian regulation, cell cycle, ion transport, and apoptosis and belonged to either the Biological Process (BP) or Cellular Component (CC) ontological groups. These pathways play a critical role in cellular homeostasis and are tightly associated with oncogenic evolution, metabolic maladaptation and infections. Additionally, lipid and steroid metabolic enrichment suggests that the compounds that are studied could regulate the processes that are often co-opted in tumorigenesis and viral pathogenesis.

In the Cellular Component (CC) category, enriched terms were mainly associated with the membrane, cytoplasm, and endoplasmic reticulum, with additional representation in synaptic regions, microsomes, and postsynaptic membranes. This distribution indicates that most target proteins are membrane-bound or cytoplasmic, which is particularly relevant for drug–target interactions, as membrane proteins—especially receptors and transporters—represent key therapeutic targets.

The Molecular Function (MF) category was enriched mainly in receptor activity, transferase activity and kinase activity and especially in G protein-coupled receptor (GPCR) signalling pathways. The critical functional clusters included serine/threonine kinases, oxidoreductases, tyrosine kinases, and monooxygenases, all of which play important roles in signalling cascades, metabolic, and immune responses regulation. Together, these findings provide a multifaceted model of biological regulation, which combines metabolic control, apoptotic responses, and host-pathogen interactions, and, therefore, supports the principles of network pharmacology and emphasises the clinical utility of the discussed compounds in the context of cancer, metabolism, and infections.

3.4 Molecular Docking Study

Molecular docking studies were done to assess the binding efficiency of selected phytoconstituents (A1–A5) with the target proteins IL6, GSK3β, and PPARG. The docking scores with interaction profiles elucidated the binding affinities and possible inhibition modalities of the compounds. Out of the screened ligands, compound A2 appeared to possess the most cost-effective binding energies over the three targets,

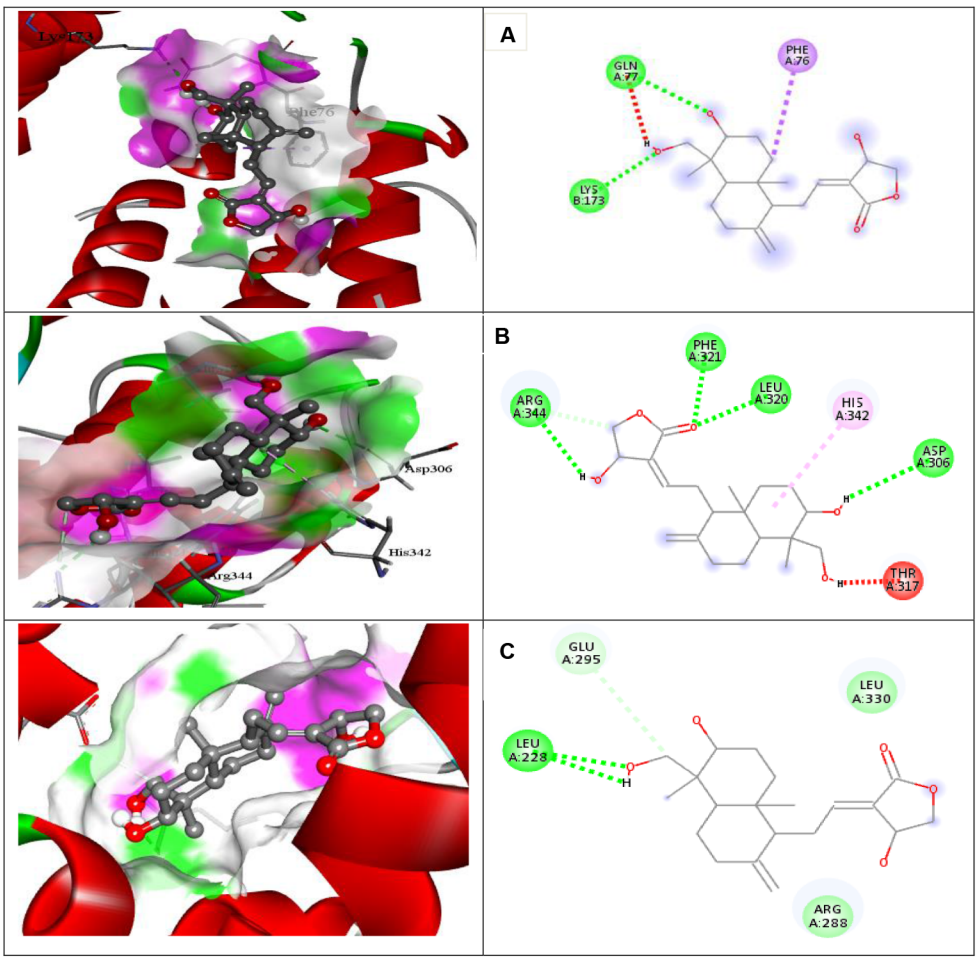


Figure 6. **(A).** 3D and 2D interaction of Andrographolide(A2) with IL6 protein; **(B).** 3D and 2D interaction of Andrographolide (A2) with GSK3β protein; **(C).** 3D and 2D interaction of Andrographolide (A2) with PPARG protein.

Table 4. Molecular docking results of the Phytoconstituents with the target protein IL6

Compound Code	IL6 Protein Docking Score (Kcal/mol)	Amino Acid Interaction
A1	-5.4	Pi-Alkyl interaction: PRO B:141
A2	-8.4	H bond interaction: GLY B:77, LYS B:173; Pi-Sigma interaction: PHE B: 76
A3	-5.6	Pi-Alkyl interaction: LYS A: 48
A4	-6.0	Pi-Alkyl interaction: PHE A: 76
A5	-5.5	H bond interaction: MET B: 69; Pi-Sigma interaction: PHE B: 76

proposing its possible development as a multi-target modulator (Figure 6).

For the IL6 protein, compound A2 exhibited the strongest binding affinity with a docking score of -8.4 kcal/mol (Table 4). It formed significant hydrogen bond interactions with GLY B:77 and LYS B:173, along with a pi-sigma interaction with PHE B:76, indicating a stable and specific binding conformation within the IL6 active site. In contrast, other compounds such as A4 (-6.0 kcal/mol), A3 (-5.6 kcal/mol), A5 (-5.5 kcal/mol), and A1 (-5.4 kcal/mol) showed comparatively moderate affinities, primarily driven by pi-alkyl interactions with residues like PRO B:141, LYS A:48, and PHE A:76. The dominance of hydrophobic contacts in these cases

Table 5. Molecular docking results of the phytoconstituents with the target protein GSK3β

Compound Code	GSK3B Protein Docking Score (Kcal/mol)	Amino Acid Interaction
A1	-5.4	Pi-Alkyl interaction: ARG A: 141
A2	-8.8	H bond interaction: ARG A: 344, PHE A: 321, LEU A: 320, ASP A: 306, Pi- Alkyl interaction: HIS A: 342
A3	-6.4	Pi-Alkyl interaction: CYS A: 199, ASN A: 186; Pi- Alkyl interaction: ALA A: 83, ILE A: 62, LEU A: 188
A4	-6.2	Pi-Alkyl interaction: LEU A: 188, ALA A: 83, CYS A: 199, VAL A: 70, ILE A: 62
A5	-7.4	Pi-Alkyl interaction: CYS A: 199, LYS A: 85, VAL A: 70, LEU A: 132, ALA A: 83, LEU A: 188, ILE A: 62, TYR A: 134

Table 6. Molecular docking results of the phytoconstituents with the target protein PPARG

Compound Code	PPARG Protein Docking Score(Kcal/mol)	Amino Acid Interaction
A1	-7.1	Pi-Alkyl interaction: PHE A: 226, MET A: 329, ALA A: 292
A2	-8.4	H bond interaction: LEU A: 228, GLU A:
A3	-7.6	Pi-Alkyl interaction: LEU A: 465, LEU A: 453, LYS A: 457
A4	-7.7	H bond interaction: LEU A: 228, Pi-Alkyl interaction: ALA A:
A5	-8.4	H bond interaction: GLU A: 343, SER A: 342 Pi-Alkyl interaction: LEU A: 330, ILE A: 326, MET A: 329

suggests relatively less stable complexes, underscoring A2's superior binding profile.

When docked against GSK3β, compound A2 has the lowest docking score, a docking score of -8.8 kcal/mol (Table 5). It hydrogen bonded with ARG A:344, PHE A:321, LEU A:320 and ASP A:306 and was bound by nonpolar and polar interactions to bind with high affinity. It was also demonstrated that A5 was associated with a binding energy (-7.4 kcal/mol) and a number of interactions with the residues CYS A:199, LYS A:85 and TYR A:134. Docking score -6.4 and -6.2 kcal/mol of interaction with ALA A:83, ILE A:62 and LEU A:188, respectively, demonstrated moderate stability of the interaction with these amino acids. It had the least interaction with a value of -5.4 kcal/mol with A1, which depicts a low degree of affinity with GSK3β. These results underscore the potential of A2 and A5 as the potential GSK3β inhibitors with therapeutic potential for the inflammatory and neurodegenerative pathways.

The docking results against PPARG revealed that compounds A2 and A5 exhibited the strongest binding affinities, each with docking scores of −8.4 kcal/mol (Table 6). Compound A2 formed hydrogen bond interactions with LEU 228 and GLU residues, supporting its interaction with polar residues important for PPARG activation. In contrast, A5 established both hydrogen bonds (GLU 343 and SER 342) and hydrophobic π-alkyl interactions with LEU 330, ILE 326, and MET 329, indicating a stable ligand–receptor complex.

Other compounds displayed moderate binding affinities, including A4 (−7.7 kcal/mol), A3 (−7.6 kcal/mol), and A1 (−7.1 kcal/mol), primarily mediated through hydrophobic interactions involving residues such as LEU 465, ALA 292, and MET 329. Collectively, these results suggest that while all tested compounds interact with PPARG to some extent, A2 and A5 demonstrate superior binding profiles toward this nuclear receptor.

Overall, compound A2 consistently showed strong binding affinities toward IL6, GSK3β, and PPARG, supported by stable hydrogen bonding and hydrophobic interactions. Compound A5, on the other hand, appeared to exhibit dual-target potential, particularly toward GSK3β and PPARG. Residues such as LEU, GLU, LYS, and PHE emerged as key

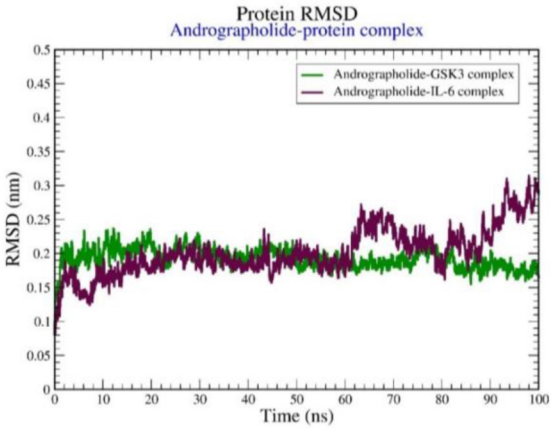


Figure 7. RMSD (nm) profiles of protein–ligand complexes over 100 ns: Andrographolide– GSK3β (green) and Andrographolide–IL-6 (brown).

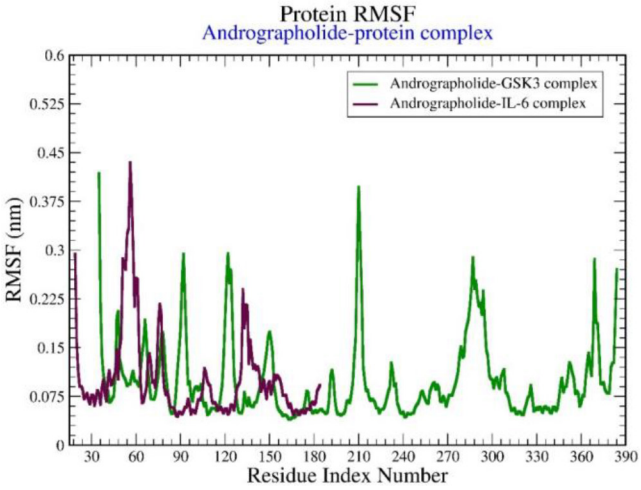


Figure 8. RMSF (nm) of protein residues for Andrographolide–GSK3β (green) and Andrographolide–IL-6 (brown).

contributors to ligand stabilisation within the binding pockets, highlighting the relevance of these compounds for further experimental evaluation.

3.5 Molecular Dynamics (MD) Simulations Study

To evaluate the binding behaviour of Andrographolide with GSK3β and IL-6 proteins, molecular dynamics (MD) simulations of 100 ns were performed on two complexes: Andrographolide– GSK3β and Andrographolide–IL-6.

The RMSD trajectories of the Andrographolide–GSK3β complex (green) and Andrographolide–IL-6 complex (brown) diverged over the course of the simulation, as seen in Figure 7. The Andrographolide–GSK3β complex exhibited relatively stable dynamics throughout the trajectory, with RMSD values fluctuating within a narrow range of approximately 0.18–0.22 nm. The complex remains well-balanced and converged throughout the simulation period. It also shows that ligand binding does not cause any meaningful alterations to the backbone conformation of the protein. This behaviour shows that GSK3β can easily change its shape to fit with andrographolide. The Andrographolide–IL-6 complex, on the other hand, changed shape more often, especially after about 60 ns, when the RMSD values started to increase and eventually reached approximately 0.32 nm at the end of the simulation. The rising RMSD trend suggests that the interaction is becoming less stable. This could be because the complex is undergoing partial conformational changes or is less stable over longer simulation times. However, the IL-6 complex was stable enough in the early stages (0–50 ns). The RMSD analysis reveals that, while complexed with GSK3β, andrographolide has greater stability than with IL-6. These results suggest that GSK3β is a structurally more appropriate target for the binding of andrographolide, and that the IL-6 complex may undergo a binding mode that is insufficiently stabilised or only temporarily stabilised.

To study the flexibility and dynamic stability of protein residues upon ligand binding, the root mean square fluctuation (RMSF) of the backbone atoms was determined for both complexes. Figure 8 shows that the RMSF profiles of the Andrographolide–GSK3β complex (green line) and the Andrographolide–IL-6 complex (brown line) exhibit different patterns of fluctuations across the residues. The Andrographolide–GSK3β complex displayed moderate fluctuations, with noticeable peaks around residues 50–70 and 120, while most regions maintained fluctuations below 0.2 nm. These are localised increases that are associated with flexible loop regions, which tend to be more dynamic than organised α-helices and β-sheets. Generally, the comparatively reduced variation in most residues demonstrates that Andrographolide binding provides stability to the GSK3β backbone.

Conversely, the Andrographolide–IL-6 complex exhibited larger fluctuations, especially in the region

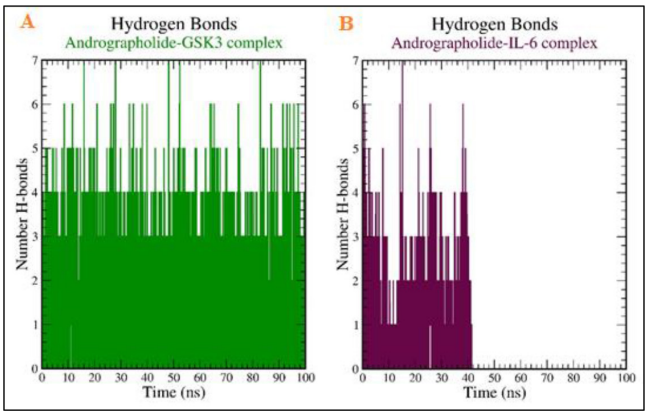


Figure 9. Number of hydrogen bond contacts formed by Andrographolide with **(A).** GSK3β and **(B).** IL-6 proteins.

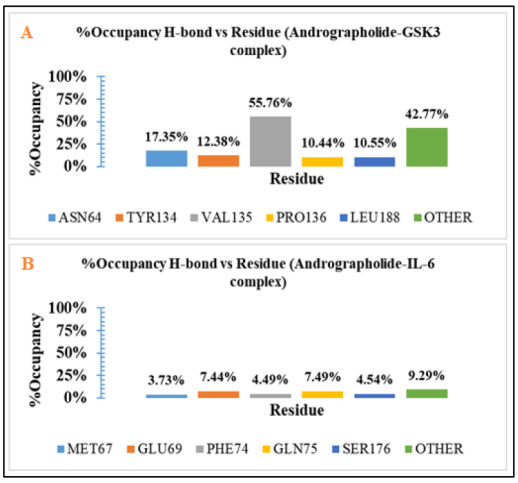


Figure 10. Percentage occupancy histograms of hydrogen bond interactions for Andrographolide with **(A).** GSK3β and **(B).** IL-6 proteins.

between residues 40–70, where the RMSF values reached maxima above 0.35 nm. The IL-6 fragments were partially stable (with fluctuations around 0.15 nm), but the high peaks indicate increased conformational flexibility, which may be due to weaker stabilisation of the ligand. This pronounced flexibility of IL-6 residues suggests that Andrographolide binding does not stabilise the protein structure uniformly, but instead induces localised structural rearrangements.

Stability and strength of interactions between Andrographolide and the two target proteins, GSK3β and IL-6, were investigated using hydrogen bonding analysis throughout the 100 ns MD simulations. Figure 9 demonstrates the number of hydrogen bonds formed over the simulation trajectory. In the case of the Andrographolide–GSK3β complex (green plot), the ligand remained constant at 3–5 hydrogen bonds at all times, with sporadic peaks of up to 6 hydrogen bonds. The existence of this concentration of hydrogen bonds throughout the 100-ns simulation time serves as evidence of strong and stable complex formation between Andrographolide and GSK3β. This balance is consistent with the results of the Root Mean Square Deviation (RMSD) as well as Root Mean Square Fluctuation (RMSF) analyses, and thus emphasises the critical role of hydrogen bonding in stabilising the complex and reducing conformational variability in the protein.

In comparison, a lower number of hydrogen bonds in the Andrographolide–IL-6 complex, as shown in the brown plot, was characterised by pronounced instability. Oscillations in hydrogen bond formation were observed, with transient peaks of four to five bonds, followed by a significant decrease after approximately 40–50 ns. The rapid attenuation of persistent hydrogen bonds indicates a weaker and lower-affinity interaction between Andrographolide and IL-6. This finding is consistent with the higher RMSF values observed for IL-6, where the absence of stable hydrogen bonding likely contributes to increased residue flexibility and overall destabilisation of the complex.

Taken collectively, these findings indicate that Andrographolide forms more favourable hydrogen-bond interactions with GSK3β compared to IL-6, supporting the conclusion that GSK3β is a more favourable binding partner. The molecular-level evidence for increased stability and binding affinity is reflected in the persistent hydrogen-bond network observed in the Andrographolide–GSK3β complex.

Stability and strength of interactions between Andrographolide and the two target proteins, GSK3β and IL-6, were investigated using hydrogen bond analysis throughout the 100 ns MD simulations. The number of hydrogen bonds formed during the simulation trajectory is shown in Figure 10. In the Andrographolide–GSK3β complex (green plot), the ligand consistently maintained 3–5 hydrogen bonds, with occasional peaks of up to 6 hydrogen bonds. These interactions persisted throughout the simulation, indicating strong and stable binding between Andrographolide and GSK3β. This observation is consistent with the RMSD and RMSF

results and highlights the importance of hydrogen bonding in stabilising the complex and limiting protein conformational fluctuations. In contrast, the Andrographolide–IL-6 complex (brown plot) exhibited fewer and less stable hydrogen bonds. Oscillations in hydrogen bond formation were observed, with transient peaks of 4–5 hydrogen bonds followed by a sharp decline after approximately 40–50 ns. The rapid loss of persistent hydrogen bonds suggests weaker and more short-lived interactions between Andrographolide and IL-6. This behaviour is consistent with the elevated RMSF values observed for IL-6, where the absence of stable hydrogen bonding likely contributes to increased residue flexibility and overall structural instability of the complex. Collectively, these findings indicate that Andrographolide forms more favourable hydrogen bond interactions with GSK3β than with IL-6, supporting the conclusion that GSK3β is a more favourable binding partner. Molecular-level evidence for increased stability and binding affinity is reflected in the persistent hydrogen bond network observed in the Andrographolide–GSK3β complex, suggesting that GSK3β may represent a more advantageous molecular target for Andrographolide binding.

4. Conclusion

The present study revealed that *D. cinerea* has a multi-target therapeutic potential based on the usage of a combined computational framework targeting the pathology of Alzheimer's disease. High-throughput screening using preliminary high-throughput screening and GC–MS profiling revealed 134 metabolites, with andrographolide being the most promising lead compound. The analysis of network pharmacology offered mechanistic information about the interdependence of the roles of neuroinflammation, dysregulation of metabolic processes, and tau-related pathology, which involved the multifunctional targets IL6, PPARG, and GSK3β. Andrographolide was found to have the best binding affinity to GSK3β. Moreover, the 100-ns molecular dynamics simulations revealed that the andrographolide–GSK3β complex showed a high degree of structural stability, with low root-mean-square deviation and stable hydrogen-bond interactions. Taken together, these results provide strong *in silico* evidence that *D. cinerea*, especially andrographolide, can act as a multi-target regulator of important pathways in Alzheimer's disease, thereby forming a concrete molecular basis for future experimental validation and therapeutic development.

5. Acknowledgement

The authors acknowledge the facilities and support provided by Vels Institute of Science, Technology and Advanced Studies (VISTAS), Pallavaram, Chennai, Tamil Nadu, India, for carrying out this research.

6. References

1. He Z, Zhang H, Hu G, Qiao Y, Yin C, Li J, Lin H, Wu A, Qin D, Law BY, Hu G, Yu L. The current status, trends, and challenges of AD and other dementias in Asia (1990–2036). Front Public Health. 2025; 13:1583339. https://doi.org/10.3389/fpubh.2025.1583339 PMid: 40556904 PMCid: PMC12185285.
2. Twiss E, McPherson C, Weaver DF. Global diseases deserve global solutions: AD. Neurol Int. 2025; 17:92. https://doi.org/10.3390/neurolint17060092 PMid: 40559330 PMCid: PMC12196516.
3. Villain N, Michalon R. What is AD? An analysis of nosological perspectives from the 20th and 21st centuries. Eur J Neurol. 2024; 31:e16302. https://doi.org/10.1111/ene.16302 PMid: 38618742 PMCid: PMC11464395.
4. Calabrese M, Preziosa P, Scalfari A, Colato E, Marastoni D, Absinta M, Battaglini M, De Stefano N, Di Filippo M, Hametner S, Howell OW. Determinants and biomarkers of progression independent of relapses in multiple sclerosis. Ann Neurol. 2024; 96:1. https://doi.org/10.1002/ana.26913 PMid: 38568026.
5. Nandi A, Counts N, Chen S, Seligman B, Tortorice D, Vigo D, Bloom DE. Global and regional projections of the economic burden of AD and related dementias from 2019 to 2050: a value of statistical life approach. E Clinical Medicine. 2022; 51:101547. https://doi.org/10.1016/j.eclinm.2022.101580 PMid: 35898316 PMCid: PMC9310134.
6. Korczyn AD, Grinberg LT. Is Alzheimer's disease a disease? Nat Rev Neurol. 2024; 20:245-251. https://doi.org/10.1038/s41582-024-00940-4 PMid: 38424454 PMCid: PMC12077607.
7. Andrews SJ, Renton AE, Fulton-Howard B, Podlesny-Drabiniok A, Marcora E, Goate AM. The complex genetic architecture of AD: novel insights and future directions. E Bio Medicine. 2023; 90:104509. https://doi.org/10.1016/j.ebiom.2023.104511 PMid: 36907103 PMCid: PMC10024184.
8. Gong CX, Dai CL, Liu F, Iqbal K. Multi-targets: an unconventional drug development strategy for AD. Front

Aging Neurosci. 2022; 14:837649. https://doi.org/10.3389/fnagi.2022.837649 PMid: 35222001 PMCid: PMC8864545.
9. Li Q, Rubin L, Silva M, Li S, Yang C, Lazarovici P, Zheng W. Current progress on neuroprotection induced by *Artemisia*, *Ginseng*, *Astragalus*, and *Ginkgo* traditional Chinese medicines for the therapy of AD. Oxid Med Cell Longev. 2022; 2022:3777021. https://doi.org/10.1155/2022/3777021 PMid: 35746960 PMCid: PMC9213169.
10. Zhao L, Zhang H, Li N, Chen J, Xu H, Wang Y, Liang Q. Network pharmacology, a promising approach to reveal the pharmacology mechanism of Chinese medicine formula. J Ethnopharmacol. 2023; 309:116306. https://doi.org/10.1016/j.jep.2023.116306 PMid: 36858276.
11. Xin WA, WA ZY, Li S. TCM network pharmacology: a new trend towards combining computational, experimental and clinical approaches. Chin J Nat Med. 2021; 19(1):1-11. https://doi.org/10.1016/S1875-5364(21)60001-8 PMid: 33516447.
12. Hopkins AL. Network pharmacology: the next paradigm in drug discovery. Nat Chem Biol. 2008; 4:682-690. https://doi.org/10.1038/nchembio.118 PMid: 18936753 PMCid: PMC9878685.
13. Mazimba O, Kwape TE, Gaobotse G. *Dichrostachys cinerea*: ethnomedicinal uses, phytochemistry and pharmacological activities—a review. Nat Prod J. 2022; 12:20. https://doi.org/10.2174/2210315511666210806144540
14. Lin X, Li X, Lin X. A review on applications of computational methods in drug screening and design. Molecules. 2020; 25:1375. https://doi.org/10.3390/molecules25061375 PMid: 32197324 PMCid: PMC7144386.
15. Noor F, Tahir ul Qamar M, Ashfaq UA, Albutti A, Alwashmi AS, Aljasir MA. Network pharmacology approach for medicinal plants: review and assessment. Pharmaceuticals. 2022; 15:572. https://doi.org/10.3390/ph15050572 PMid: 35631398 PMCid: PMC9143318.
16. Liu Q, Zhang D, Wang B, Zhao W, Zhang T, Sutcharitchan C, Li S. Network pharmacology: advancing the application of large language models in traditional Chinese medicine research. Sci Tradit Chin Med. 2025; 3:113-123. https://doi.org/10.1097/st9.0000000000000073
17. Zhang P, Zhang D, Zhou W, Wang L, Wang B, Zhang T, Li S. Network pharmacology: towards the artificial intelligence-based precision traditional Chinese medicine. Brief Bioinform. 2024; 25:bbad518. https://doi.org/10.1093/bib/bbad518 PMid: 38197310 PMCid: PMC10777171.
18. Sen U, Almeida D, da Silveira TFF, Pires TSP, Añibarro-Ortega M, Mandim F, Barros L, Ferreira ICFR, Pereira H, Fernandes A. Exploring the bioactive properties of hydroethanolic cork extracts of *Quercus cerris* and *Quercus suber*. Processes. 2024; 12:1579. https://doi.org/10.3390/pr12081579
19. de Moura FBR, Ferreira BA, Deconte SR, Landim BC, Justino AB, Aro AA, Espindola FS, Rodrigues RAF, Ribeiro DL, Araújo FA, Tomiosso TC. Wound healing activity of the hydroethanolic extract of the leaves of *Maytenus ilicifolia* Mart. ex Reis. J Tradit Complement Med. 2021; 11:446-456. https://doi.org/10.1016/j.jtcme.2021.03.003 PMid: 34522639 PMCid: PMC8427480.
20. Vinothkanna A, Prathiviraj R, Sivakumar TR, Ma Y, Sekar S. GC-MS and network pharmacology analysis of the Ayurvedic fermented medicine, *Chandanasava*, against chronic kidney and cardiovascular diseases. Appl Biochem Biotechnol. 2023; 195:2803-2828. https://doi.org/10.1007/s12010-022-04242-7 PMid: 36418713 PMCid: PMC9684947.
21. Al-Raddadi TM, Bahaffi SO, Alk-Hateeb LA. Phytochemical analysis and compound profiling of *Boerhavia elegans* stem extract using GC-MS. Anal Sci Adv. 2025; 6:e70011. https://doi.org/10.1002/ansa.70011 PMid: 40123830 PMCid: PMC11929968.
22. Asif A, Ishtiaq S, Kamran SH, Waseem R, Fatima SF, Rehman S. UHPLC-MS and GC-MS phytochemical profiling, amelioration of pain and inflammation with chloroform extract of *Funaria hygrometrica* Hedw. via modulation of inflammatory biomarkers. Inflammopharmacology. 2023; 31:1879-1892. https://doi.org/10.1007/s10787-023-01207-y PMid: 37010719.
23. Balkrishna A, Joshi M, Varshney Y, Verma S, MPR, Nain P, Varshney A. In-depth phytochemical profiling of *Roscoea purpurea* (Kakoli): comparative UHPLC-MS/QToF and GC-MS/MS analysis of supercritical CO2 fluid- and conventional solvent-based extractive processes. J Pharm Biomed Anal. 2024; 251:116444. https://doi.org/10.1016/j.jpba.2024.116444 PMid: 39197202.
24. Basit A, Ahmad S, Khan KUR, Naeem A, Usman M, Ahmed I, Shahzad MN. Chemical profiling of *Justicia vahlii* Roth. (*Acanthaceae*) using UPLC-QTOF-MS and GC-MS analysis and evaluation of acute oral toxicity, antineuropathic and antioxidant activities. J Ethnopharmacol. 2022; 287:114942. https://doi.org/10.1016/j.jep.2021.114942 PMid: 34968664.
25. Aati HY, Attia HA, Alanazi AS, Al Tamran LK, Wanner JK. Phytochemical characterization utilizing HS-SPME/GC-MS: exploration of the antioxidant and enzyme inhibition properties of essential oil from Saudi *Artemisia absinthium* L. Pharmaceuticals. 2024; 17:1460. https://doi.org/10.3390/ph17111460 PMid: 39598372 PMCid: PMC11597886.
26. Fatima SW, Alam S, Khare SK. Molecular and structural insights of β-boswellic acid and glycyrrhizic acid as potent SARS-CoV-2 envelope protein inhibitors. Phytomedicine Plus. 2022; 2:100241. https://doi.org/10.1016/j.phyplu.2022.100241 PMid: 35403092 PMCid: PMC8840829.
27. Surya PV, Radhakrishnan N, Vasantha-Srinivasan P, Veeramani C, El Newehy AS, Alsaif MA, Al-Numair KS. *In silico* analysis of selected nutrition rich fruit of bunch berry (*Lantana camara*) constituents as human acetylcholinesterase (hAchE), carbonic anhydrase II (hCA-II) and carboxylesterase 1 (hCES-1) inhibitory agents. Saudi J Biol Sci. 2023; 30:103847. https://doi.org/10.1016/j.sjbs.2023.103847 PMid: 37961045 PMCid: PMC10638019.

28. Tyagi S, Mishra R, Mazumder A, Mazumder R, Singh G, Pandey P. Synthesis, *in silico* screening, and biological evaluation of novel pyridine congeners as anti-epileptic agents targeting AMPA (α-amino-3-hydroxy-5-methylisoxazole) receptors. Chem Biol Drug Des. 2024; 103:e14498. https://doi.org/10.1111/cbdd.14498 PMid: 38453241.
29. Jovanović D, Filipović A, Janjić G, Lazarević-Pašti T, Džambaski Z, Bondžić BP, Bondžić AM. Targeting AD: evaluating the efficacy of C-1 functionalized N-aryl-tetrahydroisoquinolines as cholinergic enzyme inhibitors and promising therapeutic candidates. Int J Mol Sci. 2024; 25:1033. https://doi.org/10.3390/ijms25021033 PMid: 38256107 PMCid: PMC10816625.
30. Mansouri N, Benslama O, Lekmine S, Tahraoui H, Ola MS, Zhang J, Amrane A. Computational exploration of bacterial compounds targeting arginine-specific mono-ADP-ribosyl-transferase 1 (ART1): a pathway to novel therapeutic anticancer strategies. Curr Issues Mol Biol. 2025; 47:634. https://doi.org/10.3390/cimb47080634 PMid: 40864788 PMCid: PMC12384204.
31. Chandak SM, Kumbhare MR. Evaluation, characterization of antioxidant activity for novel benzothiazole derivatives. Zhongguo Ying Yong Sheng Li Xue Za Zhi. 2025; 41:e20250010. https://doi.org/10.62958/j.cjap.2025.010 PMid: 40533394.
32. Shah AJ, Dar MY, Adnan M, Varma T, Agarwal D, Garg P, Mir RH, Meena R, Masoodi MH. Integration of phytochemical profiling and computational approaches to evaluate the neuroprotective potential of *Nardostachys jatamansi* in AD. Biotechnol Rep. 2025; 45:e00881. https://doi.org/10.1016/j.btre.2025.e00881 PMid: 40027104 PMCid: PMC11872466.
33. Benramdane H, Benariba N, Silva CFM, Catarino MD, Bartolomeu M, Fekhikher Z, Pinto DCGA. Phytochemical profile, antioxidant, anti-Alzheimer, and α-glucosidase inhibitory effect of Algerian *Peganum harmala* seeds extract. Chem Biodivers. 2024; 21:e202401308. https://doi.org/10.1002/cbdv.202401308 PMid: 39072993.
34. Mahomoodally MF, Picot-Allain MCN, Zengin G, Llorent-Martínez EJ, Abdullah HH, Ak G, Senkardes I, Chiavaroli A, Menghini L, Recinella L, Brunetti L, Leone S, Orlando G, Ferrante C. Phytochemical analysis, network pharmacology and *in silico* investigations on *Anacamptis pyramidalis* tuber extracts. Molecules. 2020; 25:2422. https://doi.org/10.3390/molecules25102422 PMid: 32455936 PMCid: PMC7288046.
35. Ahmed SR, Khojah H, Aldera M, Alsarah J, Alwaghid D, Hamdan L, Aljuwair H, Alshammari M, Albalawi H, Aldekhail R, Alazmi A, Qasim S. Deciphering the skin anti-aging and hair growth promoting mechanisms of *Opophytum forskahlii* seed oil via network pharmacology. Int J Mol Sci. 2025; 27:277. https://doi.org/10.3390/ijms27010277 PMid: 41516153 PMCid: PMC12785290.
36. Gao K, Chen Z, Zhang N, Jiang P. High throughput virtual screening and validation of plant-based EGFR L858R kinase inhibitors against non-small cell lung cancer: an integrated approach utilizing GC-MS, network pharmacology, docking, and molecular dynamics. Saudi Pharm J. 2024; 32:102139. https://doi.org/10.1016/j.jsps.2024.102139 PMid: 39139718 PMCid: PMC11318564.
37. Sharma B, Yadav DK. Metabolomics and network pharmacology in the exploration of the multi-targeted therapeutic approach of traditional medicinal plants. Plants. 2022; 11:3243. https://doi.org/10.3390/plants11233243 PMid: 36501282 PMCid: PMC9737206.
38. Kavey MRH, Hossain MA, Shohag MSR, Ansari IA, Ansari SA, Alkahtani HM, Hossain A, Rahman MH. Multi-target therapeutic potential of Neem (*Azadirachta indica*) phytochemicals in AD: an integrative network pharmacology and molecular dynamics simulation approach. In Silico Pharmacol. 2025; 13:147. https://doi.org/10.1007/s40203-025-00434-1 PMid: 41113166 PMCid: PMC12534210.
39. Zhang H, Zhang Y, Li Y, Wang Y, Yan S, Xu S, Deng Z, Yang X, Xie H, Li J. Bioinformatics and network pharmacology identify the therapeutic role and potential mechanism of melatonin in AD and *rosacea*. Front Immunol. 2021; 12:756550. https://doi.org/10.3389/fimmu.2021.756550 PMid: 34899707 PMCid: PMC8657413.
40. Jiang M, Chi J, Qiao Y, Wang J, Zhang Z, Liu J, Sheng X, Yuan L. Ginsenosides Rg1, Rb1 and rare ginsenosides: promising candidate agents for Parkinson's disease and AD and network pharmacology analysis. Pharmacol Res. 2025; 212:107578. https://doi.org/10.1016/j.phrs.2025.107578 PMid: 39756554.
41. Kotha S, S B, Kulkarni VM, SRS, B HK, R H. An *in silico* approach: identification of PPAR-γ agonists from seaweeds for the management of AD. J Biomol Struct Dyn. 2021; 39:2210-2229. https://doi.org/10.1080/07391102.2020.1747543 PMid: 32216605.
42. Zhang Y, Lv S, Huang P, Xiao L, Lin N, Huang E. Network pharmacology study on the mechanism of berberine in AD model. npj Sci Food. 2025; 9:16. https://doi.org/10.1038/s41538-025-00378-y PMid: 39900946 PMCid: PMC11790853.
43. Moulishankar A, Sankaranarayanan M, Thirugnana sambandam S, Dhamotharan J, Mohanradja D, Sivakumar PM. Identification of novel DNA gyrase inhibitor by combined pharmacophore modeling, QSAR analysis, molecular docking, molecular dynamics, ADMET and DFT approaches. Acta Trop. 2024; 260:107460. https://doi.org/10.1016/j.actatropica.2024.107460 PMid: 39527993.
44. Murugan S, Moulishankar A, Palanivel S, Kumaradoss KM, Thirugnanasambandam S. Computational drug discovery of nitroimidazole compounds targeting

Ddn protein of *Mycobacterium tuberculosis*: insights from QSAR modeling, ADMET, molecular docking, and molecular dynamics simulation studies. Med Nov Technol Devices. 2025; 100406. https://doi.org/10.1016/j.medntd.2025.100406

45. Di S, Han L, An X, Kong R, Gao Z, Yang Y, Wang X, Zhang P, Ding Q, Wu H, Wang H. *In silico* network pharmacology and *in vivo* analysis of berberine-related mechanisms against type 2 diabetes mellitus and its complications. J Ethnopharmacol. 2021; 276:114180. https://doi.org/10.1016/j.jep.2021.114180 PMid: 33957209.
46. Essa AF, Teleb M, El-Kersh DM, El Gendy AE, Elshamy AI, Farag MA. Natural acylated flavonoids: their chemistry and biological merits in context to molecular docking studies. Phytochem Rev. 2023; 22:1469-1508. https://doi.org/10.1007/s11101-022-09840-1
47. Moulishankar A, Sundarrajan T. Pharmacophore, QSAR, molecular docking, molecular dynamics and ADMET study of trisubstituted benzimidazole derivatives as potent anti-tubercular agents. Chem Phys Impact. 2024; 8:100512. https://doi.org/10.1016/j.chphi.2024.100512
48. Das SK, Mahanta S, Tanti B, Tag H, Hui PK. Identification of phytocompounds from *Houttuynia cordata* Thunb. as potential inhibitors for SARS-CoV-2 replication proteins through GC-MS/LC-MS characterization, molecular docking and molecular dynamics simulation. Mol Diversity. 2022; 26:365-388. https://doi.org/10.1007/s11030-021-10226-2 PMid: 33961167 PMCid: PMC8103070.

Author Contribution

Prabhakar V: Conceptualisation, methodology, investigation, data curation, software, formal analysis, visualisation, and writing—original draft preparation; A. Vijayalakshmi: Supervision, validation, resources, project administration, and writing—review and editing. All authors have read and agreed to the published version of the manuscript.